RSC Advances

PAPER

View Article Online
View Journal | View Issue

Cite this: *RSC Adv.*, 2019, **9**, 38772

The synergetic effect of a structure-engineered mesoporous SiO_2–ZnO composite for doxycycline adsorption†

Danya Huang, Ying Zhang, Jingjing Zhang, Hongli Wang, Minggang Wang, Chen Wu, Daowen Cheng, Yue Chi* and Zhankui Zhao*

The design and synthesis of an efficient adsorbent for antibiotics-based pollutants is challenging due to the unique physicochemical properties of antibiotics. The development of a mesoporous SiO_2–ZnO composite is a novel way to achieve excellent adsorption efficiency for doxycycline hydrochloride (DOX) in aqueous solutions due to the engineered highly open mesoporous structure and the ZnO-modified framework. Unlike the traditional method of obtaining mesoporous composites by post-synthesis techniques, the novel one-step method developed in this study is both effective and environment-friendly. The adsorption mechanism based on the novel synergetic effect between SiO_2 and ZnO was demonstrated through several experiments. SiO_2 led to the creation of a 3D open framework structure that provides sufficient space and rapid transport channels for adsorption, ensuring rapid adsorption kinetics. A higher number of active sites and enhanced affinity of the contaminants are provided by ZnO, ensuring high adsorption capacity. The mesoporous SiO_2–ZnO could be easily regenerated without a significant decrease in its adsorption efficiency. These results indicate that the developed strategy afforded a simple approach for synthesizing the novel mesoporous composites, and that mesoporous SiO_2–ZnO is a possible alternative adsorbent for the removal of DOX from wastewater.

Received 6th October 2019
Accepted 15th November 2019

DOI: 10.1039/c9ra08106b

rsc.li/rsc-advances

1. Introduction

Pharmaceutical and personal care products (PPCPs) have become a recognized class of products containing high-risk water and environmental pollutants.[1–3] Among the various types of PPCPs, antibiotics are one of the most commonly recognized, posing a major safety threat to human physiological health and aquatic ecology.[4,5] In aquatic ecological environments, the risk of antibiotic pollutants is mainly reflected by the impact on aquatic organisms[6–8] and in the emergence and spread of resistant genes through biological generation, community succession, and ultimately the destruction of ecosystem balance.[7,9,10]

Adsorption has always been a primary choice for the removal of antibiotic pollutants due to its efficiency, low cost of operation, and low energy consumption.[11] However, commonly used adsorbents including activated carbon, clay minerals, and biochar have several limitations to be used for antibiotics adsorption, namely, low adsorption capacity, slow pollution uptake, and poor reusability.[12] Therefore, it is necessary to develop novel high-performance adsorbents to overcome these challenges.

Mesoporous SiO_2-based materials possess high surface area, large pore volume, tunable pore sizes, stable and interconnected frameworks,[13,14] as well as active pore surfaces for easy modification or functionalization, meeting the requirements as promising adsorbents.[15,16] However, most of these as-prepared materials demonstrate limited adsorption efficiency. Thus, it is necessary to attach functional components on the pore surface or framework to generate active adsorption sites.[17] Moreover, mesoporous materials usually have micrometer-sized bulk morphology with long (in micrometer) and parallel mesopore channels, resulting in inefficient mass transport and poor pore accessibility.[18,19] These characteristics adversely affect their adsorption performance. Therefore, functional mesoporous SiO_2-based materials with short and accessible mesoporous channels maybe excellent candidates for use as efficient adsorbents.[20–22] However, it is still a major challenge to control the mesostructure domain, pore size, and morphology of mesoporous materials.

Recently, remarkable progress has been achieved in the field of adsorption on metal oxides.[23–25] However, the adsorption performance of these was hindered by their low surface area due to particle aggregation.[26–28] In general, there are two main strategies to increase the surface area and accessible to active

Key Laboratory of Advanced Structural Materials of Ministry of Education, College of Material Science and Engineering, Changchun University of Technology, Changchun 130012, China. E-mail: yuechi@ccut.edu.cn; zhaozk@ccut.edu.cn; Fax: +86 431 85716644; Tel: +86 431 85716644

† Electronic supplementary information (ESI) available. See DOI: 10.1039/c9ra08106b

adsorption sites thus enhancing the adsorption properties of metal oxides. One of these is the preparation of porous metal oxides by template methods. Although this strategy can both increase the surface area and expose more active adsorption sites,[29,30] its high costs, complicated multi-step manufacturing procedure, and the fragile framework of the resulting porous metal oxides limit its practical applications.[31] The other strategy focuses on enhancing the adsorption efficiency through dispersing metal oxides on the porous support by a post-synthesis process.[32,33] Despite the successful dispersion and reduced agglomeration of metal oxides nanoparticles[34–36] as a result of this method, the loading of metal oxides in pore channels may lead to an inhomogeneous distribution of components[37] and a remarkable perturbation of the pore size, surface area, and pore volume, all of which restrain the adsorption capacity. Therefore, it is of great importance and interest to develop new strategies to both exert the advantages of mesostructure and controllably prepare mesoporous adsorbents with easily accessible surface, thereby enhancing adsorption efficiency.[38,39]

Among the currently available metal oxides, ZnO is regarded as an important material, featuring advantages in terms of costs, environmental friendliness, as well as wide spectrum absorption. In this paper, we demonstrated a simple one-pot synthesis of mesoporous SiO_2–ZnO composite as an advanced adsorbent for the removal of doxycycline hydrochloride (DOX). Unlike traditional methods of obtaining mesoporous composites by complicated multi-step manufacturing procedure, the one-step method developed in this study is facile and efficient. More importantly, this one-step strategy can effectively control the mesostructure and morphology of mesoporous SiO_2–ZnO composite, thus a synergetic effect between SiO_2 and ZnO can be formed, promising an excellent performance in adsorption. This study provides valuable insights into the development of mesoporous adsorbents for environmental remediation.

2. Materials and methods

2.1. Materials

Doxycycline hydrochloride (DOX, MW = 480.90, chemical formula $C_{22}H_{24}N_{20}HCl$), triethanolamine (TEA), cyclohexane, tetraethoxysilane (TEOS) were purchased from Sinopharm. The other chemicals including $Zn(NO_3)_2 \cdot 6H_2O$, cetyltrimethyl ammonium bromide (CTAB) were purchased from Aladdin. High purified water from a Millipore MilliQ water purification system was used in all the experiments. All chemicals employed in the experiments were purchased at analytic purity and used.

2.2. Preparation of mesoporous SiO_2–ZnO composite

6 g CTAB and 0.18 g TEA dissolved in 60 g H_2O at 60 °C for 1 h and simultaneously stirred at 150 rpm using a heater/magnetic stirrer, and then 0.59 g of $Zn(NO_3)_2 \cdot 6H_2O$ was added into the solution stirred under 60 °C for 20 min. After that, a mixed solution of 16 mL of cyclohexane and 4.2 g of TEOS was added to the above solution and stirred at 60 °C for 15 h. The resulting solution was transferred into a Teflon-lined stainless-steel autoclave, which was sealed and heated at 100 °C for 10 h and naturally cooled to room temperature. The white particles were collected and washed with ethanol and deionized water, and dried under vacuum at 60 °C for 8 h. Finally, to remove CTAB and obtain mesoporous composites, the as-prepared powder was calcined at 550 °C for 6 h with a heating rate of 5 °C min^{-1}.

For comparison, mesoporous silica was prepared without the addition of $Zn(NO_3)_2 \cdot 6H_2O$ under the same condition as that of mesoporous SiO_2–ZnO and denoted as mesoporous SiO_2 (for details, see ESI†).

2.3. Characterization methods

The morphology of the as-prepared nanocomposite was observed by the scanning electron microscope (SEM, JEOL JSM-5600), energy disperse Spectroscopy (EDS), and transmission electron microscopy (TEM, JEM-2000). The surface chemical properties of samples were measured using Fourier transform infrared spectrum (FTIR, Bio-Rad, FTS 6000), the wavelength of 4000–470 cm^{-1} is measured by the squash technique, while the wavelength of 470–420 cm^{-1} in the inset is measured by the ATR method. The nitrogen adsorption and desorption isotherms were measured at 77 K on a Micromeritics ASAP 2020 plus HD88 instrument (Micromeritics Instrument Corp, Norcross, GA). The Brunauer–Emmett–Teller (BET) specific surface area was calculated using desorption data. The pore size distribution curves were calculated based on the analysis of the desorption branch of the isotherm using the Barrett–Joyner–Halenda algorithm. X-ray diffraction (XRD) patterns were collected using a Bruker D8 Advance X-ray diffractometer to identify the crystal and channel structure with a CuKα X-ray source operating at 9 kV and 200 mA (9 kV and 200 mA for small-angle X-ray scanning). UV-visible absorption spectra were recorded using a UV-visible spectrophotometer (Cary-5000) to monitor the absorption process. XPS is a spectroscopic method for analyzing the electronic structure of a solid surface and the chemical composition of surface components by irradiating a solid material with X-rays and measuring the photoelectron energy caused by AlKα as a radiation source.

2.4. Adsorption batch experiment

Accurately prepare several volumes of 100 mg L^{-1} DOX solution, dilute it to 10–100 mg L^{-1}, scan with UV-vis at a wavelength of 200–800 nm at 600 nm min^{-1}, and obtain the corresponding absorbance at 274 nm. The standard curve equation is drawn by taking the different concentrations of DOX as the abscissa and the corresponding absorbance as the ordinate (Fig. S1†).

To avoid photodegradation, all sample conical flasks were wrapped by tin foil in all the batch experiments. A stock solution (200 mg L^{-1}) of DOX was always freshly prepared by dissolving 0.2 g of DOX into 1000 mL distilled water during all the experiments. Different DOX concentrations used in batch experiments were obtained through diluting the stock solution. 100 mg L^{-1} was the initial concentration of DOX solution. The batch experiments for sorption of DOX were carried out in 100 mL conical flasks containing 50 mg of mesoporous SiO_2–ZnO and 100 mL DOX solution, then shaken with a speed of

150 rpm for 24 h at 25 °C. The DOX solution pH was adjusted by adding negligible volumes of 0.1 M NaOH or HCl. At predetermined time, the mixture was drawn and separated by centrifuging. The remaining concentration of DOX in the supernatant was determined on a UV-visible spectrophotometer (Cary-5000) at wavelength (k_{max}) of 274 nm using standard curve equation. Adsorption efficiency E (%) and the adsorption capacity q_e (mg g^{-1}) of DOX were calculated using the following equations:

$$q_e = \frac{V(C_0 - C_e)}{m} \quad (1)$$

$$E = \frac{(C_0 - C_e) \times 100\%}{C_0} \quad (2)$$

where C_0 (mg L^{-1}) and C_e (mg L^{-1}) represent the initial and final concentrations of DOX in the aqueous phase, respectively. V (L) stands for the volume of solution, and m (g) is the mass of sorbent.[40]

To study the regeneration ability of mesoporous SiO_2–ZnO, 100 mg of mesoporous SiO_2–ZnO was added to 200 mL of DOX solution with the concentration of 100 mg L^{-1}. Since methanol has a strong polarity, it is often used as the detergent for mineral surface organic substances and can effectively remove organic matter and thus reproduce the adsorbent. Mesoporous SiO_2–ZnO loaded with DOX was treated with a methanol solution (60%) under ultrasonication for 1 h. The product was collected with the help of centrifugation, followed by repeated washing with deionized water and ethanol. Finally, the product was dried at 50 °C. We repeated the above procedure for four cycles.

3. Results and discussion

3.1. Characterization of mesoporous SiO_2–ZnO composite

A mesoporous SiO_2–ZnO composite with a 3D open framework was prepared by a simple one-pot co-assembly of CTAB, TEOS, and $Zn(NO_3)_2 \cdot 6H_2O$, followed by hydrothermal aging and calcination. The obtained mesoporous SiO_2–ZnO is composed of highly uniform mesoporous nanospheres with a mean particle size of 59.9 nm (Fig. 1a). What's more, the mesoporous SiO_2–ZnO nanospheres have good dispersibility and uniform size distribution, and the mass fractions of Si, O and Zn are 37.12%, 51.14%, 5.32%, respectively (Fig. S2†). This morphology makes mesoporous SiO_2–ZnO have short mesopore channels that can lead to efficient mass transport and good pore accessibility, positively affecting its adsorption performance. A reinforced concrete-like framework structure for mesoporous SiO_2–ZnO was obtained due to the high cross-linking degree of the SiO_2 source, which resulted in a highly porous and highly open mesostructure. The highly open mesopore channels can be clearly observed through the Fig. 1b. The wide-angle XRD pattern of the mesoporous SiO_2–ZnO composite showed diffraction peaks for ZnO at $2\theta = 31.69°$, 34.54°, 36.21°, 47.57°, 56.74°, 62.95°, 67.88° and 69.14°, which corresponded to the (100), (002), (101), (102), (110), (103), (112), and (201) orientation planes, respectively (Fig. 2). This confirmed the wurtzite structure of ZnO according to the Joint Committee on Powder Diffraction Standards Card No. 36-1451.[41,42] A broad peak at a 2θ value of 23° related to amorphous SiO_2 structure was also observed. The wurtzite phase can be seen when compared to the pattern of ZnO-free mesoporous SiO_2, implying the existence of ZnO particles in mesoporous SiO_2–ZnO. The N_2 adsorption–desorption isotherms of the obtained mesoporous SiO_2 and SiO_2–ZnO nanospheres exhibit a type IV with H_3 hysteresis loop, indicating the typical irregular mesoporous structure of the material (Fig. 3).[43] As can be seen from Table 1, compared to the mesoporous SiO_2, the BET surface area and total pore volume of mesoporous SiO_2–ZnO are calculated to be approximately 435.898 m^2 g^{-1} and 1.258 cm^3 g^{-1}, respectively, have not significantly reduced, indicative of the high porosity of mesoporous SiO_2–ZnO. The pore size distribution of mesoporous SiO_2–ZnO reveals the bimodal mesopores at the mean values of 3.306 nm and 14.268 nm, also very close to mesoporous SiO_2. According to previous studies,[44,45] the loading of metal oxides in the mesoporous materials should in theory lead to the remarkable perturbation of the surface area and pore volume. However, as shown in Fig. 3 and Table 1, no such phenomenon

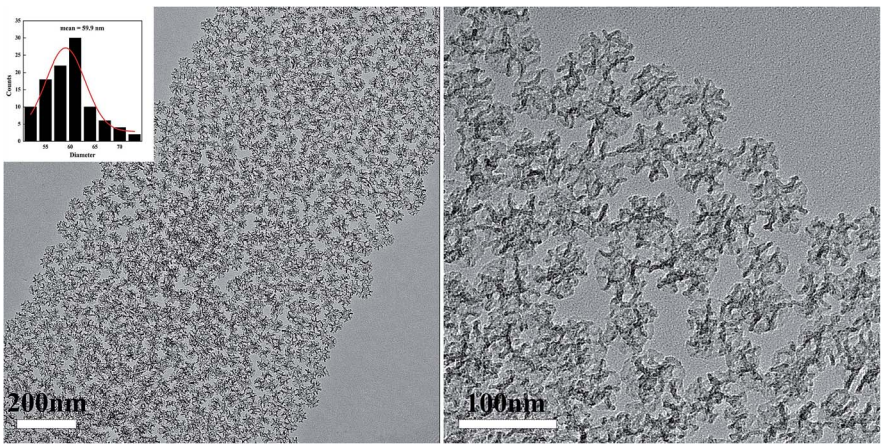

Fig. 1 TEM image of mesoporous SiO_2–ZnO. Inset describes the size distribution histogram of mesoporous SiO_2–ZnO.

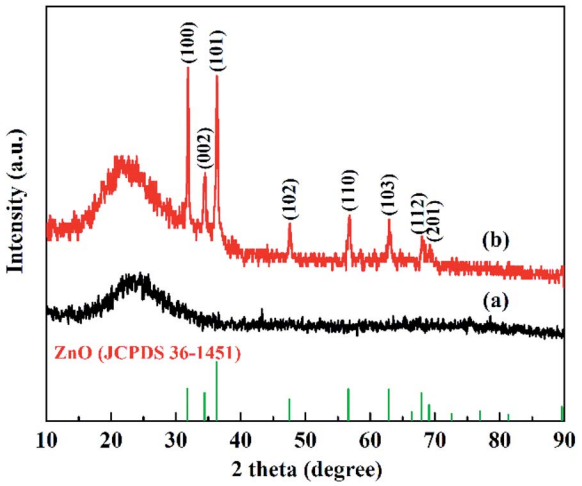

Fig. 2 XRD patterns of mesoporous SiO_2 (a) and SiO_2–ZnO (b).

occurred in this case, because the developed one-pot method has an adequate control over nanostructure construction; this can lead to the introduction of well-dispersed, small-sized ZnO particles during the fabrication of mesoporous frameworks. All these results confirm that mesoporous SiO_2–ZnO nanospheres with a highly open mesoporous structure and homogeneously dispersed ZnO particles can be synthesized by the one-pot method.

FTIR transmission spectra of mesoporous SiO_2–ZnO and ZnO-free mesoporous SiO_2 were carried out in Fig. 4A. The bands are associated with the condensed SiO_2 network, assigned to the asymmetric and symmetric stretching vibrations of Si–O–Si framework are at 1228, 1087, 806, and 445 cm^{-1}. The band centered at 969 cm^{-1} indicates the presence of perturbing or defect groups, and could be attributed to asymmetric stretching of Si–O bond neighboring surface silanol groups. This band appeared at 969 cm^{-1} in the ZnO-free mesoporous SiO_2, but degenerated to the shoulder of the 1087 cm^{-1} band in the mesoporous SiO_2–ZnO, implying that less surface

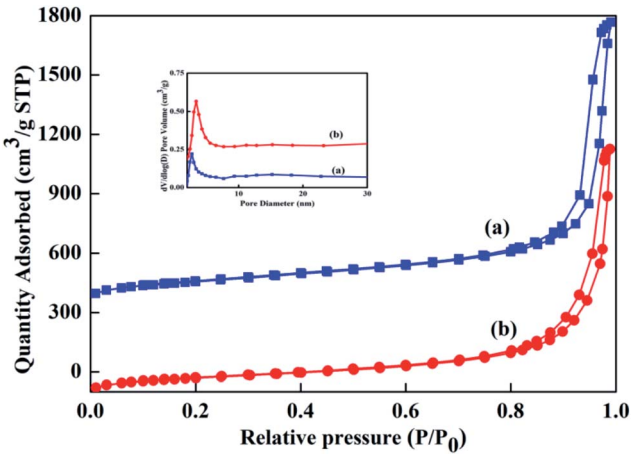

Fig. 3 N_2 adsorption–desorption isotherms of mesoporous SiO_2 (a) and SiO_2–ZnO (b). Inset describes the pore size distribution.

Table 1 Textural properties of mesoporous SiO_2 and SiO_2–ZnO

Sample	Pore size (nm)	BET surface area ($m^2\ g^{-1}$)	Pore volume ($cm^3\ g^{-1}$)
SiO_2	2.637/13.306	468.287	1.362
SiO_2–ZnO	3.306/14.268	435.898	1.258

silanol groups are formed in the mesoporous SiO_2–ZnO in comparison with pure mesoporous SiO_2. As shown in the inset of Fig. 4A, a new absorption at 424 cm^{-1} for Zn–O bonds vibrations could be identified in the mesoporous SiO_2–ZnO, further indicating the construction of a ZnO modified framework.

To study the chemical bonding states of mesoporous SiO_2–ZnO, XPS test was carried out. The peaks at 104.5 eV; 532.8 eV; and 1022.3 eV were consistent with Si 2p, O 1s, and Zn 2p (Fig. 4B) respectively.[46] These results correspond to the EDS results seen in Fig. S2.† High-resolution XPS spectra and their accommodation to Zn $2p_{3/2}$ and O 1s are shown in Fig. 4C and D. The Zn $2p_{3/2}$ peak consisted of two subpeaks that were centered at 1020.8 eV and 1022.2 eV, respectively. These peaks could be assigned to ZnO and $Zn(OH)_2$, respectively, both of which are expected to components of ZnO. The O 1s spectrum of mesoporous SiO_2–ZnO formed three sub peaks centered at 533.3 eV, 532.4 eV, and 531.5 eV, respectively. These peaks can be assigned to O–Zn, O–Si,[47,48] and O–H. The binding energy of oxygen atoms connected to Zn, Si, and H are in the order of O–Zn > O–Si > O–H because Zn, Si, and H, with the electron-donating ability of Zn > Si > H, can conjugate with oxygen atoms. Moreover, it can be seen that the binding energy of Zn three-dimensional electrons in mesoporous SiO_2–ZnO samples is 12.9 eV (Fig. 4B), which is higher than that of pure ZnO (3.23–3.29 eV),[49] indicating the existence of Zn–O–Si bonds.[50,51] This phenomenon can be explained by the high electronegativity of Si (~1.9) compared to that of Zn (~1.65); this results in a lower Zn valence electron density in the Zn–O–Si compared with that Zn–O–Zn (pure ZnO).

3.2. Adsorption studies

In order to confirm the adsorption performance of mesoporous SiO_2–ZnO as well as to investigate the synergetic effect between SiO_2 and ZnO during adsorption, we carried out adsorption of DOX by mesoporous SiO_2–ZnO. The adsorption of DOX by mesoporous SiO_2–ZnO was monitored at 298 K and 308 K under a pH value of 3.8 (Fig. S3†). The adsorption capacities of mesoporous SiO_2–ZnO towards DOX were 104.324 and 72.168 mg g^{-1} at 298 K and 308 K, respectively. The adsorption of DOX on mesoporous SiO_2–ZnO decreased by increasing temperature, suggesting that physical adsorption characteristics may play an important role in the system.[52] It should be noted that the adsorption capacity of mesoporous SiO_2–ZnO for DOX was nearly 10 times that of ZnO-free mesoporous SiO_2 (10.5 mg g^{-1}). This significant improvement in the adsorption performance of mesoporous SiO_2–ZnO can be attributed to the strong affinity of

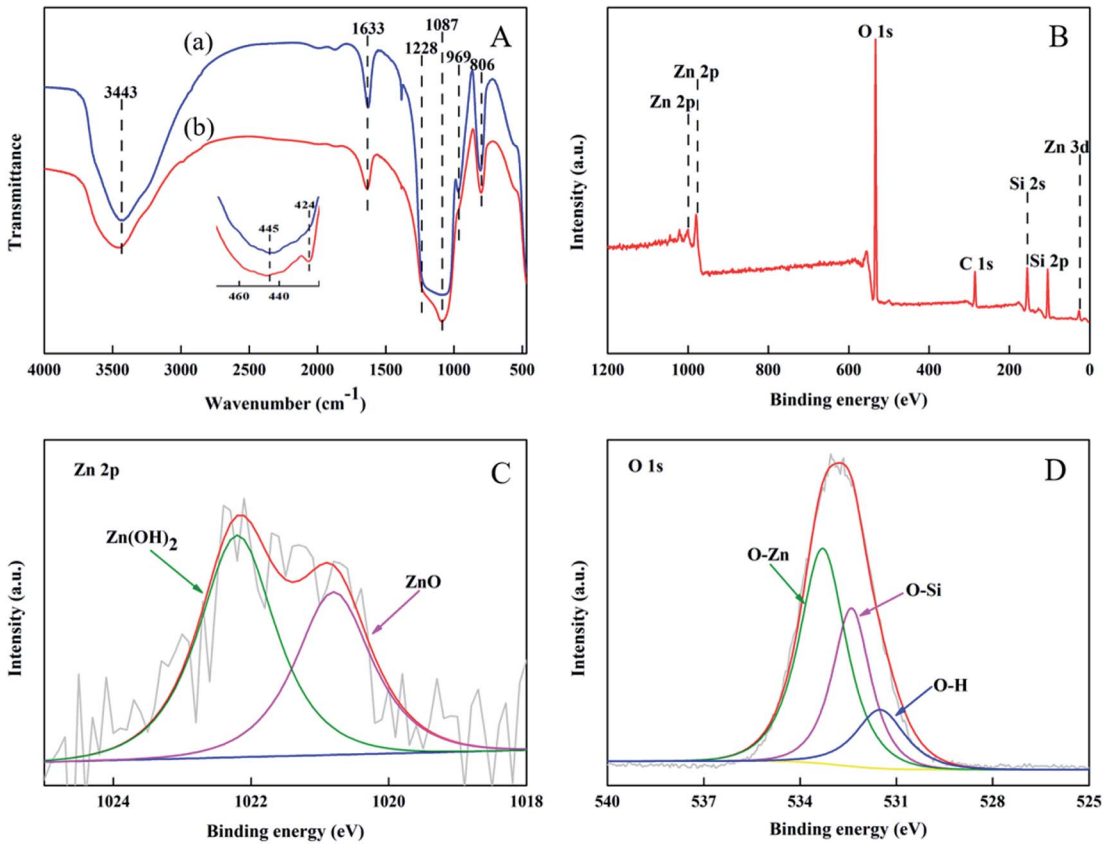

Fig. 4 FTIR spectra (A) of mesoporous SiO_2 (a) and SiO_2–ZnO (b) and XPS spectra (B–D) of mesoporous SiO_2–ZnO.

ZnO for DOX, and the electrostatic interactions seem to be an important force in the adsorption of DOX. Because of the synergetic effect between SiO_2 and ZnO, The adsorption of DOX by mesoporous SiO_2–ZnO was comprehensively improved compared to previous studies.[53–56]

In addition, the removal rate of DOX by mesoporous SiO_2–ZnO was affected by the different pH values (Fig. 5). As can be seen, the removal efficiency first increased and then decreased with the increase in the pH of the solution. Mesoporous SiO_2–ZnO exhibited high affinity for antibiotics at pH 7–8. This result suggested that the adsorption of DOX by mesoporous SiO_2–ZnO was highly pH-dependent. According to previous studies,[57] the adsorbed amount of DOX in SiO_2 materials will decrease if pH increases. Although the main component of the mesoporous SiO_2–ZnO is SiO_2 (37.12 wt%), no such phenomenon occurred in this work, further indicating that the well-dispersed ZnO particles of mesoporous SiO_2–ZnO played a predominant role in the adsorption. DOX is a kind of amphoteric compound with polyfunctional groups; its structural formula is shown in Fig. S4.† In aqueous solutions, three different groups of the molecule undergo protonation–deprotonation reactions under different pH conditions giving rise to the formation of cations, zwitterions, and anions. The deprotonated form of DOX is an anionic species at alkaline pH, while the dominant forms of DOX are zwitter ionic and cationic species at neutral and lower pH values. At acidic pH values, most of the ZnO and SiO_2 sites are protonated and presented in a positively charged form. At higher pH values, the surface of mesoporous SiO_2–ZnO will become negatively charged due to deprotonation. Therefore, the electrostatic repulsion between the DOX and mesoporous SiO_2–ZnO induced the decrease in adsorption ability at acidic and alkaline pH values.

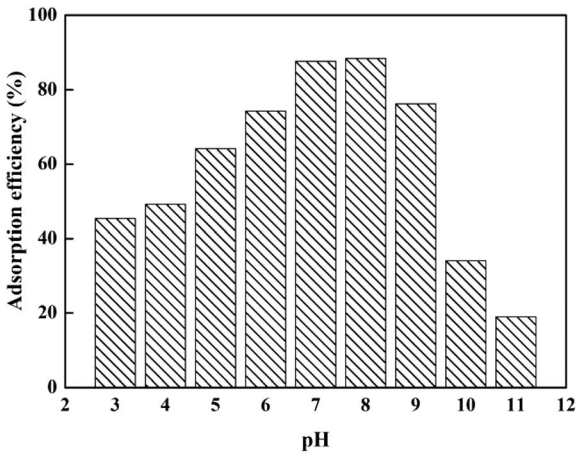

Fig. 5 Effect of the solution pH on adsorption efficiency of DOX by mesoporous SiO_2–ZnO. ($m_{sorbent}$ = 50 mg, $V_{(DOX)}$ = 100 mL, $C_{0(DOX)}$ = 100 mg L^{-1}, t = 24 h, T = 298 K).

In order to describe the adsorption isotherm and understand the intrinsic characteristics of the adsorption system, four models of Langmuir, eqn (S1);[58] Freundlich, eqn (S2);[59] Temkin, eqn (S3);[60] and Dubinin–Radushkevich (D–R), eqn (S4)–(S8)†[61,62] were used to analyze the adsorption equilibrium data at 298 K. To determine which isotherm is the best in describing the adsorption process, $(1/q_e)$ *vs.* $(1/C_e)$; $\ln(q_e)$ *vs.* $\ln(C_e)$; q_e *vs.* $\ln(C_e)$; and $\ln(q_e)$ *vs.* ε^2 plots were prepared for the Langmuir, Freundlich, Temkin, and D–R isotherms, respectively. Fig. 6 shows the linear plots, and Table 2 lists the derived parameters. The high correlation coefficient of the D–R model can explain whether this adsorption proceeds *via* physisorption or chemisorption on the basis of the sorption energy E. As shown in Table 2, the values of E were lower than 8 kJ mol^{-1} for the studied temperature, indicating that the adsorption process was predominantly physisorption.[63] On the other hand, it can be seen that the Langmuir model can also accurately reflect the adsorption isotherms under experimental conditions, which indicates the adsorption characteristics of monolayers when mesoporous SiO_2–ZnO adsorbs DOX. In addition, the Temkin model fitting degree is lower than that of the Langmuir model, but higher than that of the Freundlich model. The high fitting degree of the Temkin model reflects the existence of strong electrostatic interactions or exchanges during the adsorption process.

Table 2 Isotherm parameters for the Langmuir, Freundlich, Tempkin and Dubinin–Radushkevich (D–R) models

Langmuir model					
q_m (mg g^{-1})	K_L (L mg^{-1})	R^2	Adj. R^2	SSE	RMSE
178.571	0.032	0.984	0.981	7.951×10^{-7}	3.372×10^{-2}
Freundlich model					
K_F	n	R^2	Adj. R^2	SSE	RMSE
14.585	1.688	0.935	0.922	0.019	0.053
Tempkin model					
A_T	B	R^2	Adj. R^2	SSE	RMSE
0.286	41.219	0.965	0.958	64.291	3.031
D–R model					
β	E (kJ mol^{-1})	R^2	Adj. R^2	SSE	RMSE
28.793	0.132	0.993	0.991	1.116×10^5	126.268

The elaborate results of adsorption kinetics are presented in Fig. 7. It can be seen that the adsorption equilibrium was attained only within 90 min, a much shorter time period than

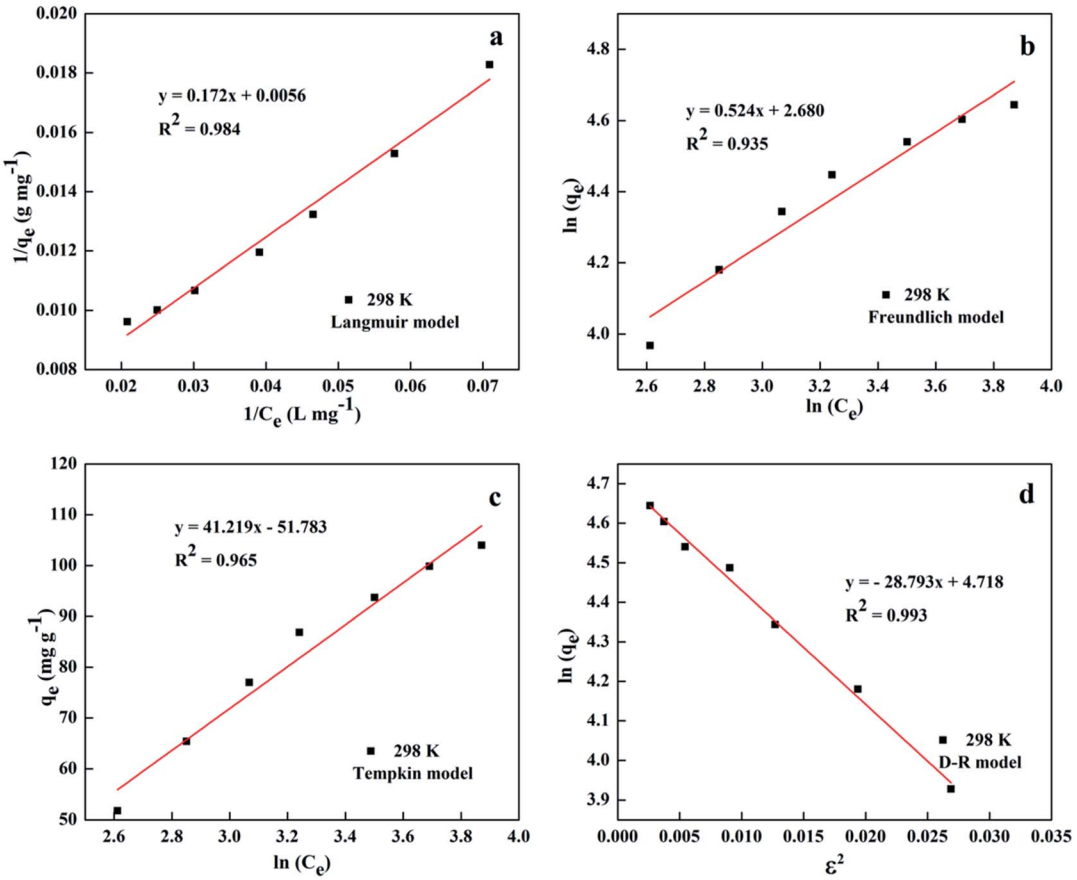

Fig. 6 Fitting of the experimental adsorption data into the Langmuir (a); Freundlich (b); Tempkin (c) and D–R (d) models.

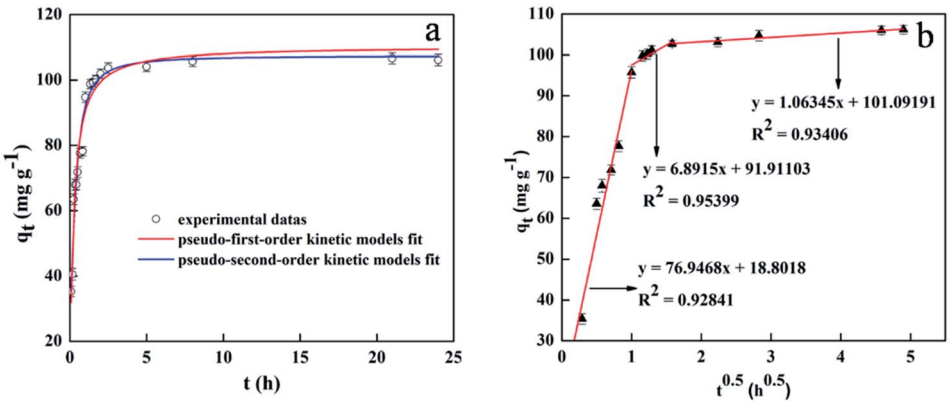

Fig. 7 Kinetics of DOX sorption onto mesoporous SiO_2–ZnO: pseudo-first-order and pseudo-second-order kinetics (a); intra-particle diffusion kinetics (b). ($m_{sorbent}$ = 100 mg, $V_{(DOX)}$ = 200 mL, $C_{0(DOX)}$ = 100 mg L^{-1}, initial pH, t = 24 h, T = 298 K).

those of other reported adsorbents.[64,65] Moreover, it should be noted that the equilibrium time needed for commercial ZnO nanoparticles (with diameters < 100 nm) was more than 24 h under the same conditions. The fast adsorption rate of mesoporous SiO_2–ZnO may be due mainly to the short mesopore channels and highly open structure, both of which increase the mass transfer and frequency of contact between adsorbents and DOX, exposing large amounts of surface area for adsorption. To further investigate the adsorption mechanism of DOX by mesoporous SiO_2–ZnO absorbent, the experimental data were analyzed by pseudo-first-order kinetic model, pseudo-second-order kinetic model, intra-particle diffusion,[66,67] and liquid-film diffusion model as seen in eqn (S9)–(S12).† The results of DOX adsorption on mesoporous SiO_2–ZnO by pseudo-first-order kinetic and pseudo-second-order kinetic models are listed in Fig. 7a. The kinetic parameters calculated from the pseudo-first-order and pseudo-second-order models are listed in Table 3. The determination coefficient of the pseudo-second-order model (R^2 = 0.999) was higher than that of the pseudo-first-order model (R^2 = 0.973). However, comparing the q_e, pseudo-first-order model fitted with the experimental data better than that of the pseudo-second-order model. Based on this data analysis, it could be deduced that both physical adsorption and chemical adsorption mechanisms can take place in this adsorption system. The better fit of the adsorption process by the pseudo-second-order model suggested that the rate-limiting step might be controlled by chemical adsorption. Under the experimental conditions, the initial adsorption rate h of the adsorption of DOX by mesoporous SiO_2–ZnO was 698.023 (mg (g h)$^{-1}$), and the time t required for the adsorption to reach half of the equilibrium adsorption was 9 min; thus it can be seen that the adsorption capacity and rate of mesoporous SiO_2–ZnO on DOX reached a higher and faster level. In order to investigate the rate-limiting step of the adsorption process, Fig. 7b displays the plots of q_t *vs.* $t^{0.5}$, exhibiting three linear stages. This indicates that the adsorption process of DOX by mesoporous SiO_2–ZnO is controlled by more than one step. The first sharper slope indicated a fast sorption of DOX on the available surface of mesoporous SiO_2–ZnO. On the second portion, intra-particle diffusion started to slow down due to the smaller pores and less sorption site availability. The third stage corresponds to the intra-particle diffusion and is attributed to the final equilibrium stage. It should be noted that three lines do not pass through the origin point, which suggests that intra-particle diffusion is not the only rate-determining step. In addition, liquid-film diffusion can also accurately reflect the adsorption process

Table 3 Pseudo-first-order, pseudo-second-order, intra-particle diffusion and liquid-film diffusion model of DOX adsorption on the mesoporous SiO_2–ZnO

	Pseudo-first-order			Pseudo-second-order			Liquid-film diffusion		
q_{exp} (mg g^{-1})	q_e (mg g^{-1})	k_1 (h^{-1})	R^2	q_e (mg g^{-1})	k_2 (g mg^{-1} h^{-1})	R^2	k_f (h^{-1})	A	R^2
104.324	78.739	1.820	0.973	105.226	0.063	0.999	1.742	−0.325	0.976

Intra-particle diffusion

	Phase one			Phase two			Phase three		
q_{exp} (mg g^{-1})	K_{d1} (mg g^{-1} h$^{-0.5}$)	C_1	R^2	K_{d2} (mg g^{-1} h$^{-0.5}$)	C_2	R^2	K_{d3} (mg g^{-1} h$^{-0.5}$)	C_3	R^2
104.324	76.948	18.804	0.928	6.892	91.913	0.954	1.063	101.092	0.934

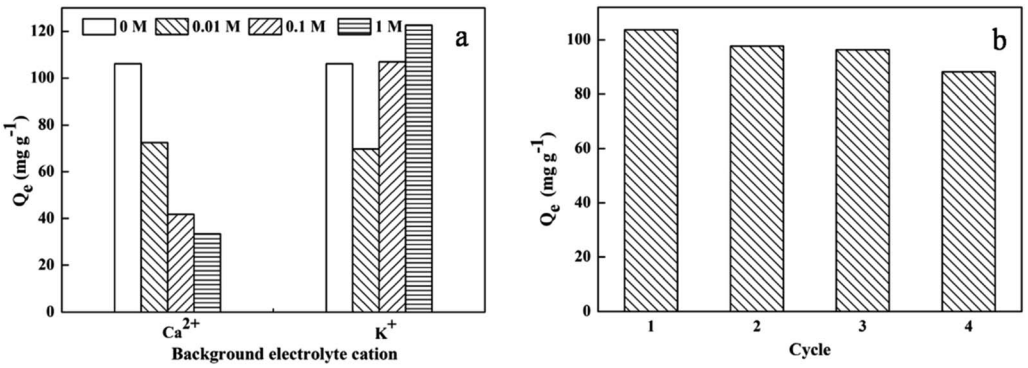

Fig. 8 Effect of ionic strength for DOX adsorption onto mesoporous SiO_2–ZnO (a) and sorption–desorption cycles of mesoporous SiO_2–ZnO (b). ($m_{sorbent}$ = 10 mg, V = 20 mL, $C_{0(DOX)}$ = 100 mg L^{-1}, T = 298 K, initial pH).

with an R^2 value of 0.976 (Table 3), suggesting that both intra-particle diffusion and liquid-film diffusion determine the adsorption process.

KCl and $CaCl_2$ were selected as ion sources to investigate the influence of ionic strength on DOX adsorption by mesoporous SiO_2–ZnO at salt concentrations of 0–1 mol L^{-1}. Fig. 8a shows that Ca^{2+} ions inhibited the adsorption of DOX on mesoporous SiO_2–ZnO. This result can be attributed to probable competition of Ca^{2+} ions with DOX to occupy the active adsorptive sites, inhibiting the electrostatic interaction between DOX and the adsorbent and thus reducing the adsorption amount. In contrast, the adsorption of DOX by mesoporous SiO_2–ZnO indicated a decline when the K^+ ion concentration was less than 0.1 mol L^{-1}; the adsorption of DOX was promoted at a high K^+ ion concentration. The cationic forms of DOX under this pH condition might participate in electrostatic competition or electrostatic repulsion with K^+ ion at low concentrations, thus leading to a decrease in the adsorption amount. When the K^+ ion concentration increased, the solubility of DOX in water decreased, facilitating the diffusion of DOX to the surface of the adsorbent. Therefore, there was an increase in the adsorption capability at a high K^+ ion concentration, suggesting that special interactions and DOX complexation might exist without electrostatic sorption.

Recycling and regeneration of an adsorbent are important factors for practical applications of the adsorbent. As shown in Fig. 8b, the adsorption efficiency decreased slightly in sequential cycles. After four regeneration cycles, the removal efficiency was still > 85%, suggesting a positive reusability and regeneration ability of mesoporous SiO_2–ZnO.

4. Conclusions

In summary, a simple one-pot strategy for preparing mesoporous SiO_2–ZnO with effective control of both mesostructure and morphology was demonstrated. The obtained mesoporous SiO_2–ZnO was composed of highly uniform mesoporous nanospheres with a highly open mesostructure, a ZnO-modified framework, and satisfactory pore accessibility. The synergetic effect between SiO_2 and ZnO was identified as lead to lead to the efficient mass transport and enhanced affinity for DOX, resulting in rapid adsorption kinetics and high adsorption capacity. The main sorption mechanisms of DOX to mesoporous SiO_2–ZnO were electrostatic interaction and surface complexation. The resulting mesoporous SiO_2–ZnO was found to regenerate efficiently and could be reused for DOX adsorption over four sequential recycle steps. This highly effective mesoporous adsorbent is a promising candidate to remove DOX and other persistent organic pollutants from water.

Conflicts of interest

There are no conflicts to declare.

Acknowledgements

This work was supported by the National Natural Science Foundation of China (51608050, 51601018 and 51671035).

References

1 H. J. An, B. N. Bhadra, N. A. Khan and S. H. Jhung, Adsorptive removal of wide range of pharmaceutical and personal care products from water by using metal azolate framework-6-derived porous carbon, *Chem. Eng. J.*, 2018, **343**, 447–454.
2 J. W. O'Brien, A. P. Banks, A. J. Novic, J. F. Mueller, G. Jiang, C. Ort, G. Eaglesham, Z. Yuan and P. K. Thai, Impact of in-Sewer Degradation of Pharmaceutical and Personal Care Products (PPCPs) Population Markers on a Population Model, *Environ. Sci. Technol.*, 2017, **51**, 3816–3823.
3 X. Bai and K. Acharya, Algae-mediated removal of selected pharmaceutical and personal care products (PPCPs) from Lake Mead water, *Sci. Total Environ.*, 2017, **581–582**, 734–740.
4 L. P. Johnson, G. E. Walton, A. Psichas, G. S. Frost, G. R. Gibson and T. G. Barraclough, Prebiotics Modulate the Effects of Antibiotics on Gut Microbial Diversity and Functioning in Vitro, *Nutrients*, 2015, **7**, 4480–4497.
5 J. Jin, T. Feng, R. Gao, Y. Ma, W. Wang, Q. Zhou and A. Li, Ultrahigh selective adsorption of zwitterionic PPCPs both in the absence and presence of humic acid: performance and mechanism, *J. Hazard. Mater.*, 2018, **348**, 117–124.

6 J. Du, H. Zhao, S. Liu, H. Xie, Y. Wang and J. Chen, Antibiotics in the coastal water of the South Yellow Sea in China: occurrence, distribution and ecological risks, *Sci. Total Environ.*, 2017, **595**, 521–527.

7 P. Valitalo, A. Kruglova, A. Mikola and R. Vahala, Toxicological impacts of antibiotics on aquatic micro-organisms: a mini-review, *Int. J. Hyg. Environ. Health*, 2017, **220**, 558–569.

8 B. T. Chu, M. L. Petrovich, A. Chaudhary, D. Wright, B. Murphy, G. Wells and R. Poretsky, Metagenomics Reveals the Impact of Wastewater Treatment Plants on the Dispersal of Microorganisms and Genes in Aquatic Sediments, *Appl. Environ. Microbiol.*, 2018, **84**, e02168.

9 P. Y. Basak, E. S. Cetin, I. Gurses and A. G. Ozseven, The effects of systemic isotretinoin and antibiotic therapy on the microbial floras in patients with acne vulgaris, *J. Eur. Acad. Dermatol. Venereol.*, 2013, **27**, 332–336.

10 S. Spycher, S. Mangold, T. Doppler, M. Junghans, I. Wittmer, C. Stamm and H. Singer, Pesticide Risks in Small Streams-How to Get as Close as Possible to the Stress Imposed on Aquatic Organisms, *Environ. Sci. Technol.*, 2018, **52**, 4526–4535.

11 M. Paredes-Laverde, J. Silva-Agredo and R. A. Torres-Palma, Removal of norfloxacin in deionized, municipal water and urine using rice (Oryza sativa) and coffee (Coffea arabica) husk wastes as natural adsorbents, *J. Environ. Manage.*, 2018, **213**, 98–108.

12 P. Hadi, M. H. To, C. W. Hui, C. S. Lin and G. McKay, Aqueous mercury adsorption by activated carbons, *Water Res.*, 2015, **73**, 37–55.

13 X. Zheng, H. Lin, J. Zheng, X. Duan and Y. Yuan, Lanthanum Oxide-Modified Cu/SiO_2 as a High-Performance Catalyst for Chemoselective Hydrogenation of Dimethyl Oxalate to Ethylene Glycol, *ACS Catal.*, 2013, **3**, 2738–2749.

14 F. Nador, E. Guisasola, A. Baeza, M. A. Villaecija, M. Vallet-Regi and D. Ruiz-Molina, Synthesis of Polydopamine-Like Nanocapsules via Removal of a Sacrificial Mesoporous Silica Template with Water, *Chem.–Eur. J.*, 2017, **23**, 2753–2758.

15 V. J. Mayani, S. V. Mayani and S. W. Kim, Simple preparation of tungsten supported carbon nanoreactors for specific applications: adsorption, catalysis and electrochemical activity, *Appl. Surf. Sci.*, 2015, **345**, 433–439.

16 J. Shen, G. Ma, J. Zhang, W. Quan and L. Li, Facile fabrication of magnetic reduced graphene oxide-$ZnFe_2O_4$ composites with enhanced adsorption and photocatalytic activity, *Appl. Surf. Sci.*, 2015, **359**, 455–468.

17 H. Zhang, L. Chen, M. Lu, J. Li and L. Han, A novel film-pore-surface diffusion model to explain the enhanced enzyme adsorption of corn stover pretreated by ultrafine grinding, *Biotechnol. Biofuels*, 2016, **9**, 181.

18 C. Z. Yu, J. Fan, B. Tian and D. Y. Zhao, Morphology development of mesoporous materials: a colloidal phase separation mechanism, *Chem. Mater.*, 2004, **16**, 889–898.

19 E. Ortel, S. Sokolov and R. Kraehnert, Influence of steel substrate roughness on morphology and mesostructure of TiO_2 porous layers produced by template-assisted dip coating, *Microporous Mesoporous Mater.*, 2010, **127**, 17–24.

20 J. G. Wang, F. Li, H. J. Zhou, P. C. Sun, D. T. Ding and T. H. Chen, Silica Hollow Spheres with Ordered and Radially Oriented Amino-Functionalized Mesochannels, *Chem. Mater.*, 2009, **21**, 612–620.

21 S. Liu, H. Zhang, X. Meng, Y. Zhang, L. Ren, F. Nawaz, J. Liu, Z. Li and F.-S. Xiao, Ordered hexagonal mesoporous silica materials (SBA-15) with additional disordered large-mesopore networks formed by gaseous expansion, *Microporous Mesoporous Mater.*, 2010, **136**, 126–131.

22 X. Zhou, H. Chen, Y. Zhu, Y. Song, Y. Chen, Y. Wang, Y. Gong, G. Zhang, Z. Shu, X. Cui, J. Zhao and J. Shi, Dual-mesoporous ZSM-5 zeolite with highly b-axis-oriented large mesopore channels for the production of benzoin ethyl ether, *Chem.–Eur. J.*, 2013, **19**, 10017–10023.

23 J. Wang, L. Xiao, S. Wen, N. Chen, Z. Dai, J. Deng, L. Nie and J. Min, Hierarchically porous SiO_2/C hollow microspheres: a highly efficient adsorbent for Congo Red removal, *RSC Adv.*, 2018, **8**, 19852–19860.

24 I. Ahmed and S. H. Jhung, Composites of metal–organic frameworks: preparation and application in adsorption, *Mater. Today*, 2014, **17**, 136–146.

25 Z. Wen, Y. Zhang, S. Guo and R. Chen, Facile template-free fabrication of iron manganese bimetal oxides nanospheres with excellent capability for heavy metals removal, *J. Colloid Interface Sci.*, 2017, **486**, 211–218.

26 W.-J. Zhang, A review of the electrochemical performance of alloy anodes for lithium-ion batteries, *J. Power Sources*, 2011, **196**, 13–24.

27 M. Peer, A. Qajar, R. Rajagopalan and H. C. Foley, On the effects of emulsion polymerization of furfuryl alcohol on the formation of carbon spheres and other structures derived by pyrolysis of polyfurfuryl alcohol, *Carbon*, 2013, **51**, 85–93.

28 T. Hiemstra, J. C. Mendez and J. Li, Evolution of the reactive surface area of ferrihydrite: time, pH, and temperature dependency of growth by Ostwald ripening, *Environ. Sci.: Nano*, 2019, **6**, 820–833.

29 Z. Liu, T. Fan, D. Zhang, X. Gong and J. Xu, Hierarchically porous ZnO with high sensitivity and selectivity to H_2S derived from biotemplates, *Sens. Actuators, B*, 2009, **136**, 499–509.

30 Y. Yan, B. Xia, Z. Xu and X. Wang, Recent Development of Molybdenum Sulfides as Advanced Electrocatalysts for Hydrogen Evolution Reaction, *ACS Catal.*, 2014, **4**, 1693–1705.

31 J. Fan, S. W. Boettcher and G. Stucky, Nanoparticle Assembly of Ordered Multicomponent Mesostructured Metal Oxides via a Versatile Sol−Gel Process, *Chem. Mater.*, 2006, **18**, 6391–6396.

32 Q. Han, L. Yang, Q. Liang and M. Ding, Three-dimensional hierarchical porous graphene aerogel for efficient adsorption and preconcentration of chemical warfare agents, *Carbon*, 2017, **122**, 556–563.

33 Q. Song, Y. Fang, Z. Liu, L. Li, Y. Wang, J. Liang, Y. Huang, J. Lin, L. Hu, J. Zhang and C. Tang, The performance of

porous hexagonal BN in high adsorption capacity towards antibiotics pollutants from aqueous solution, *Chem. Eng. J.*, 2017, **325**, 71–79.

34 M. H. Alkhraisat, C. Rueda, J. Cabrejos-Azama, J. Lucas-Aparicio, F. T. Marino, J. Torres Garcia-Denche, L. B. Jerez, U. Gbureck and E. L. Cabarcos, Loading and release of doxycycline hyclate from strontium-substituted calcium phosphate cement, *Acta Biomater.*, 2010, **6**, 1522–1528.

35 A. W. Bayeh, D. M. Kabtamu, Y.-C. Chang, G.-C. Chen, H.-Y. Chen, G.-Y. Lin, T.-R. Liu, T. H. Wondimu, K.-C. Wang and C.-H. Wang, Synergistic effects of a $TiNb_2O_7$–reduced graphene oxide nanocomposite electrocatalyst for high-performance all-vanadium redox flow batteries, *J. Mater. Chem. A*, 2018, **6**, 13908–13917.

36 Z. Liu, L. Yao, X. Pan, Q. Liu and H. Huang, A green and facile approach to the efficient surface modification of alumina nanoparticles with fatty acids, *Appl. Surf. Sci.*, 2018, **447**, 664–672.

37 I.-D. Kim, A. Rothschild and H. L. Tuller, Advances and new directions in gas-sensing devices, *Acta Mater.*, 2013, **61**, 974–1000.

38 F. Wu, W. Liu, J. Qiu, J. Li, W. Zhou, Y. Fang, S. Zhang and X. Li, Enhanced photocatalytic degradation and adsorption of methylene blue via TiO_2 nanocrystals supported on graphene-like bamboo charcoal, *Appl. Surf. Sci.*, 2015, **358**, 425–435.

39 E. M. Samsudin, S. B. Abd Hamid, J. C. Juan, W. J. Basirun and G. Centi, Synergetic effects in novel hydrogenated F-doped TiO_2 photocatalysts, *Appl. Surf. Sci.*, 2016, **370**, 380–393.

40 S. Liu, W. H. Xu, Y. G. Liu, X. F. Tan, G. M. Zeng, X. Li, J. Liang, Z. Zhou, Z. L. Yan and X. X. Cai, Facile synthesis of Cu(II) impregnated biochar with enhanced adsorption activity for the removal of doxycycline hydrochloride from water, *Sci. Total Environ.*, 2017, **592**, 546–553.

41 Y. Zhang and S.-J. Park, Stabilizing CuPd bimetallic alloy nanoparticles deposited on holey carbon nitride for selective hydroxylation of benzene to phenol, *J. Catal.*, 2019, **379**, 154–163.

42 Y. Zhang and S.-J. Park, Facile construction of MoO_3@ZIF-8 core–shell nanorods for efficient photoreduction of aqueous Cr(VI), *Applied Catalysis, B: Environmental*, 2019, **240**, 92–101.

43 Y. Zhang and S.-J. Park, Stabilization of dispersed CuPd bimetallic alloy nanoparticles on ZIF-8 for photoreduction of Cr(VI) in aqueous solution, *Chem. Eng. J.*, 2019, **369**, 353–362.

44 Y. Zhang, F. Jiang, D. Huang, S. Hou, H. Wang, M. Wang, Y. Chi and Z. Zhao, A facile route to magnetic mesoporous core–shell structured silicas containing covalently bound cyclodextrins for the removal of the antibiotic doxycycline from water, *RSC Adv.*, 2018, **8**, 31348–31357.

45 S. Hou, X. Li, H. Wang, M. Wang, Y. Zhang, Y. Chi and Z. Zhao, Synthesis of core–shell structured magnetic mesoporous silica microspheres with accessible carboxyl functionalized surfaces and radially oriented large mesopores as adsorbents for the removal of heavy metal ions, *RSC Adv.*, 2017, **7**, 51993–52000.

46 N. Huang, J. Shu, Z. Wang, M. Chen, C. Ren and W. Zhang, One-step pyrolytic synthesis of ZnO nanorods with enhanced photocatalytic activity and high photostability under visible light and UV light irradiation, *J. Alloys Compd.*, 2015, **648**, 919–929.

47 M. W. Gaultois and A. P. Grosvenor, XANES and XPS investigations of the local structure and final-state effects in amorphous metal silicates: $(ZrO_2)_x(TiO_2)_y(SiO_2)_{1-x-y}$, *Phys. Chem. Chem. Phys.*, 2012, **14**, 205–217.

48 M. Copuroglu, H. Sezen, R. L. Opila and S. Suzer, Band-bending at buried SiO_2/Si interface as probed by XPS, *ACS Appl. Mater. Interfaces*, 2013, **5**, 5875–5881.

49 R. D. Suryavanshi, S. V. Mohite, A. A. Bagade, S. K. Shaikh, J. B. Thorat and K. Y. Rajpure, Nanocrystalline immobilised ZnO photocatalyst for degradation of benzoic acid and methyl blue dye, *Mater. Res. Bull.*, 2018, **101**, 324–333.

50 X. Collard, M. El Hajj, B.-L. Su and C. Aprile, Synthesis of novel mesoporous ZnO/SiO_2 composites for the photodegradation of organic dyes, *Microporous Mesoporous Mater.*, 2014, **184**, 90–96.

51 F. Li, H. Xu, W. Xue, Y. Wang and X. Zhao, The one-pot synthesis of methylene diphenyl-4,4′-dicarbamate, *Chem. Eng. J.*, 2015, **135**, 217–222.

52 I. Turku, T. Sainio and E. Paatero, Thermodynamics of tetracycline adsorption on silica, *Environ. Chem. Lett.*, 2007, **5**, 225–228.

53 Y. Lin, S. Xu and J. Li, Fast and highly efficient tetracyclines removal from environmental waters by graphene oxide functionalized magnetic particles, *Chem. Eng. J.*, 2013, **225**, 679–685.

54 Y. K. Lv, J. Q. Zhang, Y. D. He, J. Zhang and H.-W. Sun, Adsorption-controlled preparation of molecularly imprinted hybrid composites for selective extraction of tetracycline residues from honey and milk, *New J. Chem.*, 2014, **38**, 802–808.

55 X. Zhang, B. Bai, G. Li Puma, H. Wang and Y. Suo, Novel sea buckthorn biocarbon SBC@β-FeOOH composites: efficient removal of doxycycline in aqueous solution in a fixed-bed through synergistic adsorption and heterogeneous Fenton-like reaction, *Chem. Eng. J.*, 2016, **284**, 698–707.

56 Z.-w. Zeng, S.-r. Tian, Y.-g. Liu, X.-f. Tan, G.-m. Zeng, L.-h. Jiang, Z.-h. Yin, N. Liu, S.-b. Liu and J. Li, Comparative study of rice husk biochars for aqueous antibiotics removal, *J. Chem. Technol. Biotechnol.*, 2018, **93**, 1075–1084.

57 M. Brigante and M. Avena, Biotemplated synthesis of mesoporous silica for doxycycline removal. Effect of pH, temperature, ionic strength and Ca^{2+} concentration on the adsorption behaviour, *Microporous Mesoporous Mater.*, 2016, **225**, 534–542.

58 I. Langmuir, The constitution and fundamental properties of solids and liquids, Part II.—Liquids, *J. Franklin Inst.*, 1916, **184**, 102–105.

59 S. K. Behera, J. H. Kim, X. Guo and H. S. Park, Adsorption equilibrium and kinetics of polyvinyl alcohol from

aqueous solution on powdered activated carbon, *J. Hazard. Mater.*, 2008, **153**, 1207–1214.

60 K. I. Aika and A. Ozaki, Kinetics and isotope effect of ammonia synthesis over a singly-promoted iron catalyst, *J. Catal.*, 1969, **13**, 232–237.

61 J. Ma, Y. Xiong, X. Dai and F. Yu, Coadsorption behavior and mechanism of ciprofloxacin and Cu(II) on graphene hydrogel wetted surface, *Chem. Eng. J.*, 2020, **380**, 1385–8947.

62 L. Li, J. Zhao, Y. Sun, F. Yu and J. Ma, Ionically cross-linked sodium alginate/κ-carrageenan double-network gel beads with low-swelling, enhanced mechanical properties, and excellent adsorption performance, *Chem. Eng. J.*, 2019, **372**, 1091–1103.

63 A. Rey, J. A. Zazo, J. A. Casas, A. Bahamonde and J. J. Rodriguez, Influence of the structural and surface characteristics of activated carbon on the catalytic decomposition of hydrogen peroxide, *Appl. Catal., A*, 2011, **402**, 146–155.

64 Y. Chao, W. Zhu, X. Wu, F. Hou, S. Xun, P. Wu, H. Ji, H. Xu and H. Li, Application of graphene-like layered molybdenum disulfide and its excellent adsorption behavior for doxycycline antibiotic, *Chem. Eng. J.*, 2014, **243**, 60–67.

65 Z. W. Zeng, X. F. Tan, Y. G. Liu, S. R. Tian, G. M. Zeng, L. H. Jiang, S. B. Liu, J. Li, N. Liu and Z. H. Yin, Comprehensive Adsorption Studies of Doxycycline and Ciprofloxacin Antibiotics by Biochars Prepared at Different Temperatures, *Front. Chem.*, 2018, **6**, 80.

66 M. Barkat, D. Nibou, S. Chegrouche and A. Mellah, Kinetics and thermodynamics studies of chromium(VI) ions adsorption onto activated carbon from aqueous solutions, *Chem. Eng. Process.*, 2009, **48**, 38–47.

67 A. Rodriguez, J. Garcia, G. Ovejero and M. Mestanza, Adsorption of anionic and cationic dyes on activated carbon from aqueous solutions: equilibrium and kinetics, *J. Hazard. Mater.*, 2009, **172**, 1311–1320.